




Optical absorption and energy loss spectroscopy of single-walled carbon nanotubes

María Rosa Preciado-Rivas , Victor Alexander Torres-Sánchez , and Duncan J. Mowbray ^{*}
School of Physical Sciences and Nanotechnology, Yachay Tech University, Urcuquí 100119, Ecuador



(Received 19 July 2019; revised manuscript received 27 November 2019; published 16 December 2019)

The recent development of efficient chirality sorting techniques has opened the way to the use of single-walled carbon nanotubes (SWCNTs) in a plethora of nanoelectronic, photovoltaic, and optoelectronic applications. However, to understand the excitation processes undergone by SWCNTs, it is necessary to have highly efficient and accurate computational methods to describe their optical and electronic properties, methods which have until now been unavailable. Here we employ linear combinations of atomic orbitals (LCAOs) to represent the Kohn-Sham (KS) wave functions and perform highly efficient time-dependent density functional theory (TDDFT) calculations in the frequency domain using our LCAO-TDDFT- k - ω code to model the optical absorbance and energy loss spectra and spatial distribution of the exciton charge densities in SWCNTs. By applying the GLLB-SC derivative discontinuity correction to the KS eigenenergies, we reproduce the measured E_{11} and E_{22} transitions within $\sigma \lesssim 70$ meV and the optical absorbance and electron energy loss spectra semiquantitatively for a set of 15 semiconducting and 4 metallic chirality sorted SWCNTs. Furthermore, our calculated electron hole density difference $\Delta\rho(\mathbf{r}, \omega)$ resolves the spatial distribution of the measured excitations in SWCNTs. These results open the path towards the computational design of optimized SWCNT nanoelectronic, photovoltaic, and optoelectronic devices *in silico*.

DOI: [10.1103/PhysRevB.100.235429](https://doi.org/10.1103/PhysRevB.100.235429)

I. INTRODUCTION

Single-walled carbon nanotubes (SWCNTs) have drawn attention in the field of organic electronics due to their unique physical properties, e.g., ballistic conductance, tailorable band gaps, photoluminescence, and high optical absorbance [1]. These nearly one-dimensional (1D) structures come in various chiralities, which, depending on the way they are rolled up, change their energy band gaps yielding a plethora of different absorption and conductive properties [2]. A variety of different semiconducting SWCNTs can be used to widen the range of wavelengths that can be potentially exploited in photovoltaic applications [3,4]. SWCNTs exhibit intense absorption peaks with band gaps between 0.9 and 1.5 eV and have high thermal stability [5,6]. In the case of metallic nanotubes, electronic transport occurs ballistically, meaning they can carry high currents without heating [7,8]. Furthermore, a clear advantage are the recently developed methods for separating SWCNTs based on their chirality. This provides a straightforward method for tailoring the band gap of the semiconducting layer in a solar cell.

For these reasons, SWCNTs have been widely used as additives in organic photovoltaic (OPV) devices to improve their efficiency by increasing the charge carrier mobility of conventional polymers [9,10] and dye-sensitized solar cells. In donor-acceptor hybrid cells, SWCNTs have been used to either covalently [11] or noncovalently [12] graft chromophore molecules, increasing incident photon to current efficiency (IPCE) by about 17%. SWCNTs can interact with polymers via π - π stacking, porphyrins electrostatically [13] to achieve

an IPCE of 8.4%, lipid nanodiscs, and human DNA [14]. Moreover, in many other photovoltaic devices, metallic carbon nanotubes are used as electrodes because of their ballistic conducting properties.

Spectroscopy techniques are widely used to characterize SWCNTs. The advantages of optical absorbance (OA), a specific type of spectroscopy, rely on the fact that it is nondestructive, noninvasive, and simple to perform at room temperature and under ambient pressure. For instance, photoluminescence, absorption, and resonance Raman spectroscopy are widely employed in bulk SWCNTs samples in both research [15,16] and industrial laboratories [17]. This makes spectroscopy techniques important for the development of OPVs as these methods provide insight into the properties of the materials, whether they are suitable for photovoltaic devices, and how they can be improved. For example, information about the exciton generation process can be gathered through spectroscopy techniques to make further improvements in the design of OPVs. This is because, in the case of OA, light is most often absorbed when in resonance with the band gap of the material so that the observation of absorption peaks are related to electron transitions.

Theoretical calculations of the photoabsorption processes in systems provide insight into not only how excitons are generated, but also other properties, such as the charge distribution, which can help to explain what is observed in experimental data. Some of the most commonly used methods are those based on density functional theory (DFT) [18]. DFT, based on the hypothesis that the electron density distribution completely characterizes the ground state of many electron systems, uses functionals of the spatially dependent electron density to model the ground state electronic structure and properties at the quantum mechanical level.

^{*}duncan.mowbray@gmail.com

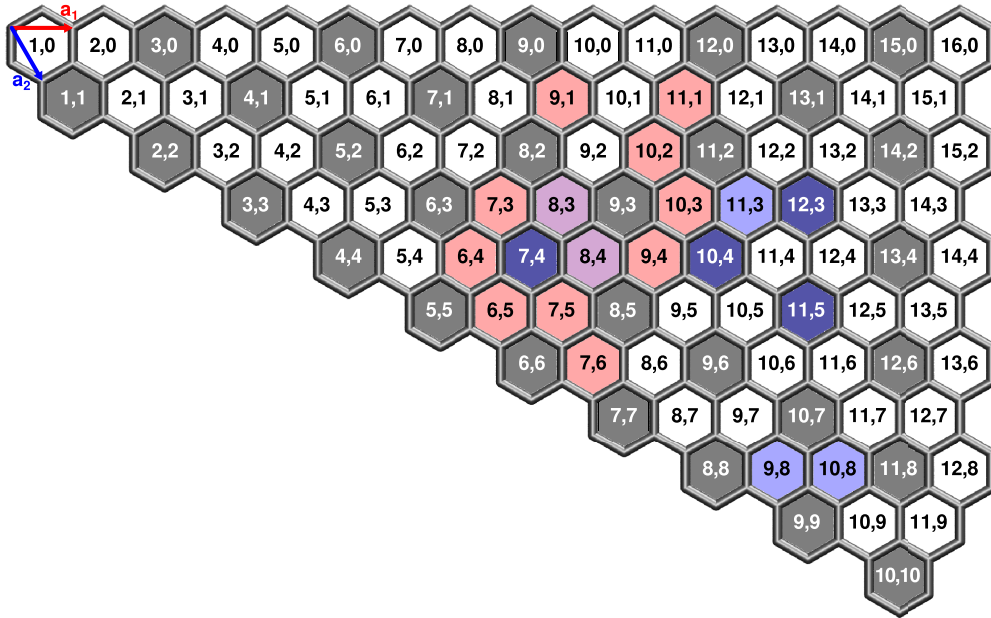


FIG. 1. SWCNT indices (m, n) of circumference vector $\mathbf{C} \equiv m\mathbf{a}_1 + n\mathbf{a}_2$ where \mathbf{a}_1 (red) and \mathbf{a}_2 (blue) are the primitive unit vectors with optical absorbance (red), electron energy loss (blue), and both (mauve) data from Refs. [24,25], respectively. Metallic tubes ($m - n = 0 \pmod{3}$) are marked in gray or dark blue.

DFT has made important contributions in material design projects by combining theory and computational methods to replace traditional, and often expensive, experiments [19,20]. For instance, DFT calculations have been done to unravel the characteristics of spectroscopy for SWCNTs with linear response time-dependent density functional theory (TDDFT) used to complement the experimental work made in Ref. [21]; additionally, estimates of the internal quantum efficiency of organic photovoltaic devices containing polymers, fullerene C_{60} , and SWCNTs have been obtained using DFT [22].

Optical selection rules for SWCNTs allow light polarized parallel to the nanotube's axis to excite intense transitions between the corresponding subbands in the valence and conduction bands. For instance, $v_1 \rightarrow c_1$ and $v_2 \rightarrow c_2$, and so on, correspond to well-defined absorption transitions between van Hove singularities with energies E_{11} and E_{22} . Metallic SWCNTs also have intense absorption peaks associated with transitions between van Hove singularities [23]. Recently, experimental measurements of chirality sorted SWCNTs have provided both optical absorbance [24] and electron energy loss spectra [25] for a large variety of SWCNTs. For this reason, SWCNTs provide experimentally relevant 1D periodic systems for benchmarking our LCAO-TDDFT- k - ω code [21,26–28].

In this work we employ linear combinations of atomic orbitals (LCAO) to represent the Kohn-Sham (KS) wave functions within time-dependent density functional theory (TDDFT) in momentum \mathbf{k} and frequency ω space, using our LCAO-TDDFT- k - ω code [21,26–28], applying the derivative discontinuity correction [29] to the KS eigenenergies. This method is applied to the set of 4 metallic and 15 semiconducting chiral SWCNTs mapped in Fig. 1, for which optical absorbance and electron energy loss spectroscopy measurements of chirality sorted samples are available from Refs. [24,25], respectively. Employing the exciton density

method implemented within our LCAO-TDDFT- k - ω code [26,28], we are able to provide a spatially resolved description of the experimentally observed transitions in metallic and semiconducting SWCNTs.

The paper is organized as follows. In Sec. II we begin by providing a brief theoretical background in Sec. II A to the derivative discontinuity correction Δ_x , the LCAO-TDDFT- k - ω method in the optical limit $\|\mathbf{q}\| \rightarrow 0^+$, and our model for the spatial distribution of the exciton charge density $\Delta\rho = \rho_e + \rho_h$, followed by a complete description of the relevant parameters employed in our DFT, LCAO-TDDFT- k - ω [26], PW-TDDFT- k - ω [30], quasiparticle (QP) G_0W_0 [31], and Bethe-Salpeter equation (BSE) [32] calculations in Sec. II B. In Sec. III we compare our results with those obtained from experiments for the 19 chiral SWCNTs studied (see Fig. 1), including the atomic and electronic structure in Sec. III A, optical absorbance spectra in Sec. III B, the E_{11} and E_{22} transitions in semiconducting SWCNTs in Sec. III C, and electron energy loss spectroscopy in Sec. III D, followed by our spatially resolved description of the electron-hole density difference for the E_{11} transition in semiconducting SWCNTs and the Drude plasmon in metallic SWCNTs in Sec. III E. Finally, concluding remarks are provided in Sec. IV. Atomic units ($\hbar = e = m_e = a_0 = 1$) have been employed throughout unless otherwise noted.

II. METHODOLOGY

A. Theoretical background

Modeling the optical absorbance or electron energy loss spectra of a material requires a proper description of its electronic structure, including the electronic band gap E_{gap} . At the Kohn-Sham (KS) level the band gap is approximated by the energy difference between the KS eigenenergies, $\Delta_{\text{KS}} = \varepsilon_{N+1} - \varepsilon_N$, where N is the number of electrons and we have

suppressed dependence on spin and k point. However, Δ_{KS} often underestimates the experimental band gap by an order of magnitude. Although the exchange and correlation (xc) potential can be tuned to obtain a better agreement of Δ_{KS} with E_{gap} , this can lead to a potential that has unphysical features, resulting in a poor description of properties other than the band gap [33]. While both hybrid functionals (HSE06 [34]) and quasiparticle methods (G_0W_0 [35–38]) often provide a sufficiently accurate description of the electronic structure, their intractability makes such methods unsuitable for large macromolecules such as the chiral SWCNTs we will study herein.

The derivative discontinuity correction to the exchange functional Δ_x has been proposed as a first-order *ab initio* correction to the KS band gap [39], where $E_{\text{gap}} \approx \Delta_{\text{KS}} + \Delta_x$. Kuisma *et al.* [29] calculated the exchange part of the derivative discontinuity Δ_x from the KS equations by using a modified version of the Gritsenko, van Leeuwen, van Lenthe, and Baerends (GLLB) xc potential [40,41]. This xc potential exhibits a step structure at the lowest unoccupied orbital when it starts to be occupied.

A newer version of this potential is called GLLB-SC, for solid and correlation, and has been shown to yield a better agreement with the experimental band gaps than LDA or GGA for solids [42]. The derivative discontinuity correction of the exchange part of the GLLB-SC functional is given by

$$\Delta_x = \frac{8\sqrt{2}}{3\pi^2} \sum_{n=1}^N (\sqrt{\varepsilon_{N+1} - \varepsilon_n} - \sqrt{\varepsilon_N - \varepsilon_n}) \times \langle \psi_{N+1} | \frac{\psi_n^* \psi_n}{\rho} | \psi_{N+1} \rangle, \quad (1)$$

where N is the number of electrons, ψ_n and ε_n are the n th Kohn-Sham (KS) wave function and eigenenergy, respectively, and we have suppressed dependence on the spin and k point.

Major advantages of employing Δ_x are both its *ab initio* nature and its efficiency. Specifically, the calculation of Δ_x requires a single-point calculation of the electronic structure for the relaxed geometry, and the summation given in Eq. (1). This makes the derivative discontinuity correction an attractive alternative to hybrid functionals or quasiparticle methods for accurately describing the electronic structure of large macromolecules.

We model the optical absorption and electron energy loss spectra using the head of the dielectric function $\varepsilon(\omega)$ from our LCAO-TDDFT- k - ω code [21,26–28], neglecting local crystal field effects. Adding the derivative discontinuity correction of the exchange part of the GLLB-SC functional Δ_x from Eq. (1) to the eigenenergies of unoccupied KS states, the dielectric function is then [21,35]

$$\varepsilon(\omega) = 1 - \frac{4\pi}{\Omega} \sum_{nm} \frac{f(\varepsilon_m) - f(\varepsilon_n)}{\omega - (\varepsilon_n - \varepsilon_m + \Delta_x) + i\eta} \times \left| \frac{\hat{\mathbf{e}}_{\mathbf{q}} \cdot \langle \psi_n | \nabla | \psi_m \rangle}{\varepsilon_n - \varepsilon_m + \Delta_x} \right|^2, \quad (2)$$

where we have suppressed spin and k -point dependence, f is the Fermi-Dirac function, $\eta \approx 25$ meV is the Lorentzian

broadening of the peaks, and $\hat{\mathbf{e}}_{\mathbf{q}}$ is a unit vector in the direction of the light's polarization $\mathbf{q} \rightarrow 0^+$.

The matrix elements in Eq. (2) are expressed using the PAW formalism as

$$\langle \psi_n | \nabla | \psi_m \rangle = \sum_{a,a'} \sum_{ij} c_{in}^{a\dagger} c_{jm}^a \langle \tilde{\phi}_i^a | \mathcal{T}^\dagger \nabla \mathcal{T} | \tilde{\phi}_j^a \rangle, \quad (3)$$

where $\tilde{\phi}_i^a$ is the i th smooth basis function centered on atom a and \mathcal{T} is the PAW transformation operator

$$\mathcal{T} = 1 + \sum_a \sum_i (|\varphi_i^a\rangle - |\tilde{\varphi}_i^a\rangle) \langle \tilde{p}_i^a|, \quad (4)$$

where φ_i^a and $\tilde{\varphi}_i^a$ are the all-electron and pseudopartial waves for state i on atom a and \tilde{p}_i^a are their smooth PAW projector functions.

Methods for calculating Eq. (3) are already implemented within DFT to obtain the forces, i.e., the expectation value of the gradient operator within the LCAO basis. For this reason, obtaining the dielectric function $\varepsilon(\omega)$ within the LCAO-TDDFT- k - ω code simply involves the multiplication of matrices that have already been calculated, i.e., the KS coefficient matrices c_{in}^a with the expectation values of the gradient operator in the PAW-corrected LCAO basis $\langle \tilde{\phi}_i^a | \mathcal{T}^\dagger \nabla \mathcal{T} | \tilde{\phi}_j^a \rangle$.

This is a very efficient method with a scaling better than $\mathcal{O}(NM^2)$ where N is the number of KS wave functions and $M \geq N$ is the total number of basis functions used in the LCAO calculation. Moreover, the implicit summation over spin, k point, and domain in Eq. (2) lends itself trivially to parallelization employing the facilities available within most DFT codes. This degree of parallelizability, as implemented within the LCAO-TDDFT- k - ω code [26,28], proved essential for performing distributed memory calculations of SWCNTs with large unit cells (~ 50 Å) employing the dense k -point sampling ($\Delta k \lesssim \frac{1}{1200}$ nm $^{-1}$) required to converge the room temperature ($\eta \approx 25$ meV) optical absorbance.

It should be noted that employing an LCAO representation to solve for the nonzero dielectric matrix elements, outside the optical limit $\mathbf{q} \rightarrow 0^+$, is unfeasible. This is because the LCAO representation does not lend itself to the efficient calculation of Fourier transforms, unlike real-space and plane-wave methods. For this reason, the LCAO-TDDFT- k - ω code's range of applicability is restricted to the optical limit with local crystal field effects neglected. However, as we shall see, this simplification, when the GLLB-SC derivative discontinuity correction is employed, leads to a semiquantitative description of optical and energy loss spectra for SWCNTs.

We model the exciton density as the electron-hole density difference $\Delta\rho(\mathbf{r}, \omega) = \rho_h(\mathbf{r}, \omega) + \rho_e(\mathbf{r}, \omega)$, where the electron/hole densities are obtained by averaging over the hole/electron position, as implemented in our LCAO-TDDFT- k - ω code [26,28]. This may be calculated using [43,44]

$$\Delta\rho(\mathbf{r}, \omega) \approx \sum_{nm} \frac{\eta^2 |\tau_{m \rightarrow n}|^2 [|\psi_m(\mathbf{r})|^2 - |\psi_n(\mathbf{r})|^2]}{[\omega - (\varepsilon_n - \varepsilon_m + \Delta_x)]^2 + \eta^2}, \quad (5)$$

where we have suppressed spin and k -point dependence and $\int \Delta\rho(\mathbf{r}, \omega) d^3\mathbf{r} = 0$. Here $|\tau_{m \rightarrow n}|^2$ are the calculated

intensities of the $m \rightarrow n$ transition from $\text{Im}[\varepsilon(\omega)]$ of Eq. (2), so that

$$\text{Im}[\varepsilon(\omega)] = \int \rho_h(\mathbf{r}, \omega) d^3\mathbf{r} = - \int \rho_e(\mathbf{r}, \omega) d^3\mathbf{r}. \quad (6)$$

In this way we take into account the relative strength of transitions and their contribution at a given frequency ω .

B. Computational details

In Fig. 1 we show the indices (m, n) of the SWCNTs for which we have performed calculations. Those marked in red are semiconducting SWCNTs with optical absorption spectra, in blue are semiconducting SWCNTs with electron energy loss spectra, in mauve are those with both optical absorption and electron energy loss spectra, and those in dark blue are metallic SWCNTs with electron energy loss spectra, as taken from Refs. [24,25].

Our density functional theory (DFT) calculations were performed using the GPAW code [30,45], based on the projector-augmented wave (PAW) method [45,46] within the atomic simulation environment (ASE) [47,48]. We have used for the SWCNTs a revised Perdew-Burke-Ernzerhof generalized gradient approximation (GGA) for solids (PBEsol) [49] for the exchange and correlation (xc) functional, and represented the Kohn-Sham (KS) wave functions using a linear combination of atomic orbitals (LCAO) [50] with a double- ζ -polarized (DZP) basis set, after performing convergence tests with basis sets of varying quality up to a quadruple- ζ -polarized (QZP) basis set, or plane waves (PWs) with a plane-wave cutoff of $E_{\text{cut}} = 340$ or 700 eV. A room temperature electronic broadening of $\eta = k_B T = 25$ meV was employed throughout.

Both the unit cell and atomic structure for each of the 19 SWCNTs studied (see Fig. 1) were relaxed until the maximum force was less than 0.05 eV/Å by including 10 Å of vacuum perpendicular to the SWCNT's axis. Periodic boundary conditions were employed only in the direction of the SWCNT axis, with the electron density and KS wave functions set to zero at the unit cell boundaries perpendicular to the SWCNT's axis. A grid spacing of $h \approx 0.2$ Å was employed and the Brillouin zone was sampled with a k -point density of $\Delta k \lesssim \frac{1}{30}$ Å⁻¹ along the SWCNT's axis.

A Harris calculation was performed for each SWCNT to increase the k -point density to $\Delta k \lesssim \frac{1}{1200}$ nm⁻¹, fixing the electron density throughout the self-consistency cycle. Such a dense k -point density was found to be necessary to converge the calculated absorbance spectra at room temperature ($\eta = k_B T = 25$ meV). In order to improve the description of the electronic gap, we employed the derivative discontinuity correction to the exchange part of the GLLB-SC functional Δ_x as provided in Eq. (1), by performing a single-point calculation for the relaxed structures with GLLB-SC.

All calculations of the dielectric function $\varepsilon(\omega)$ and electron-hole density difference $\Delta\rho(\mathbf{r}, \omega)$ were performed using either linear combinations of atomic orbitals (LCAOs) or plane waves (PWs) to represent the KS wave functions at the time-dependent density functional theory (TDDFT) level in the optical limit ($\mathbf{q} \rightarrow 0^+$) in reciprocal k space and the frequency ω domain using either our LCAO-TDDFT- k - ω code [21,26–28] or GPAW's PW-TDDFT- k - ω code [30]. In

TABLE I. Relaxed single-walled carbon nanotube (SWCNT) diameters d and unit cell lengths L in Å, numbers of atoms N_{at} per unit cell, derivative discontinuity corrections Δ_x and electronic band gaps E_{gap} in eV, and real ε_∞ and inverse ε_∞^{-1} dielectric constants.

SWCNT	d (Å)	L (Å)	N_{at}	Δ_x (eV)	E_{gap} (eV)	ε_∞	ε_∞^{-1}
(6, 4)	6.97	18.64	152	0.418	1.528	5.71	0.175
(9, 1)	7.62	40.81	364	0.417	1.476	6.27	0.159
(8, 3)	7.84	42.12	388	0.399	1.414	6.25	0.160
(6, 5)	7.60	40.83	364	0.374	1.317	6.32	0.158
(7, 3)	7.09	38.06	316	0.365	1.281	6.67	0.150
(7, 5)	8.31	44.68	436	0.360	1.273	6.51	0.154
(10, 2)	8.84	23.80	248	0.358	1.269	6.82	0.147
(9, 4)	9.17	49.33	532	0.339	1.199	6.90	0.145
(8, 4)	8.40	11.34	112	0.329	1.158	7.05	0.142
(7, 6)	8.97	48.21	508	0.315	1.113	7.16	0.140
(10, 3)	9.36	50.47	556	0.278	0.983	8.13	0.123
(11, 1)	9.16	49.35	532	0.269	0.950	8.57	0.117
(10, 8)	12.38	33.37	488	0.240	0.849	8.57	0.117
(9, 8)	11.66	63.02	868	0.246	0.869	9.62	0.104
(11, 3)	10.13	54.63	652	0.310	1.098	7.41	0.135
(11, 5)	11.22	20.20	268	–	–	–	–
(12, 3)	10.89	6.51	84	–	–	–	–
(10, 4)	9.91	8.91	104	–	–	–	–
(7, 4)	7.70	13.69	124	–	–	–	–
(10, 0)	7.96	4.30	40	0.788	1.550	3.08	0.325
(10, 10)	13.71	2.46	40	–	–	–	–

both cases we have employed a room temperature Lorentzian broadening ($\eta = 25$ meV) to the peaks and corrected the eigenenergies by the derivative discontinuity correction Δ_x from Eq. (1) when calculating the dielectric function using Eq. (2). We model the optical absorbance spectra using $\text{Im}[\varepsilon(\omega)]$ and the electron energy loss spectra using $-\text{Im}[\varepsilon^{-1}(\omega)]$ [35].

QP G_0W_0 [31] and partially self-consistent scQPGW₀ [51] calculations of the electronic band gap were performed using the PW implementation within the GPAW code [52]. We used energy cutoffs of 10, 50, or 100 eV, including eight bands per atom, and a $1 \times 1 \times 64$ k -point sampling of the Brillouin zone, consistent with Ref. [3]. The Godby-Needs plasmon-pole approximation [53–55] was employed to describe the screening W and a 1D truncation scheme for the Coulomb kernel [56] was used to remove spurious interactions with periodic images orthogonal to the SWCNT's axis. We employed an increased 16 Å of vacuum between periodic images to ensure the 1D Coulomb truncation scheme did not remove any relevant interactions within the SWCNT. Our scQPGW₀ calculations employed a mixing of 0.25 for each of the ten iterations performed to achieve self-consistency [36,37].

III. RESULTS AND DISCUSSION

A. Atomic and electronic structure

We will begin our analysis of the SWCNTs shown schematically in Fig. 1 by considering their atomic and electronic structure. As shown in Table I, this is a rather diverse selection of chiral SWCNTs, with diameters ranging from 6.97 to 12.38 Å, lengths from 6.51 to 63.02 Å, and from 84

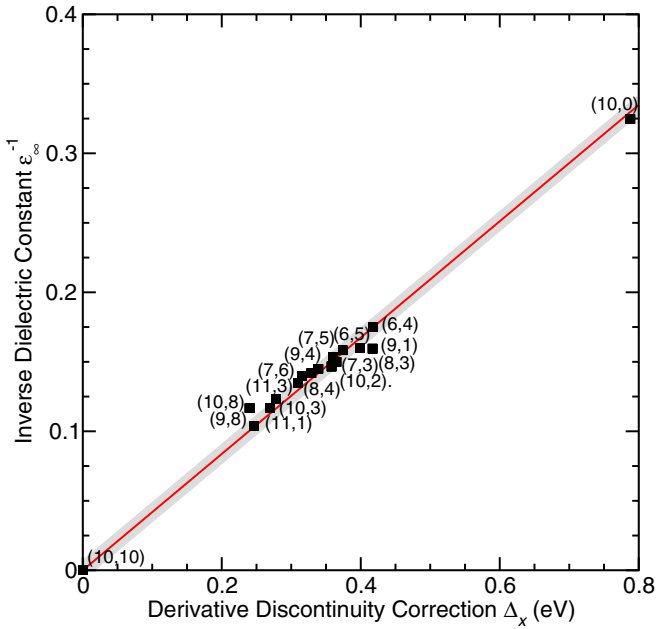


FIG. 2. LCAO-TDDFT- k - ω calculated inverse dielectric constant $\varepsilon_{\infty}^{-1}$ versus derivative discontinuity correction to the GLLB-SC exchange functional Δ_x in eV for 17 different SWCNT chiralities from Table I. A linear fit $\varepsilon_{\infty}^{-1} \approx 0.418\Delta_x$ ($r \approx 0.995$) is shown in red with standard deviations $\sigma \approx 0.007$ depicted as gray regions.

to 868 atoms per unit cell. Moreover, they exhibit different electronic properties, with 4 of them being metallic SWCNTs and the remaining 15 semiconducting SWCNTs with band gaps between 0.8 and 1.6 eV and dielectric constants between 5.7 and 9.6.

In Table I we also provide the derivative discontinuity correction of the exchange part of the GLLB-SC functional [29] Δ_x calculated using Eq. (1). These corrections have a size on average of $\sim 28\%$ of the corrected band gap ($\Delta_x \approx 0.28E_{\text{gap}}$), and are thus proportional to both the corrected band gap energy E_{gap} and the KS band gap Δ_{KS} . More specifically, for the SWCNTs considered herein, Δ_x ranges from 0.24 to 0.42 eV, as shown in Table I.

Taking into account the achiral semiconducting (10, 0) and metallic (10, 10) SWCNTs, we see from Fig. 2 that Δ_x is directly correlated with the inverse dielectric constant $\varepsilon_{\infty}^{-1}$ obtained from our LCAO-TDDFT- k - ω calculations and provided in Table I. This is significant, as previous studies have shown that the quasiparticle (QP) correction Δ_{QP} to the electronic band gap $E_{\text{gap}}^{\text{QP}} = \Delta_{\text{KS}} + \Delta_{\text{QP}}$ [36] is also directly correlated with the inverse dielectric constant of the material [38]. This is because the dielectric constant ε_{∞} describes the effective screening W of electronic levels by the material, whereas the QP energy shift Δ_{QP} replaces the xc potential V_{xc} with the frequency-dependent self-energy $\Sigma(\omega) = iGW$ normalized by a factor Z , i.e., $\Delta_{\text{QP}} \equiv Z[\Sigma(\omega) - V_{\text{xc}}]$ [36]. From this we may infer that a direct linear relationship should also exist between Δ_x and Δ_{QP} .

Since the derivative discontinuity correction Δ_x is much easier to calculate than the QP energy shift Δ_{QP} , this suggests one could use this linear relationship to estimate Δ_{QP} for the 15 semiconducting SWCNT chiralities shown in Fig. 1. By

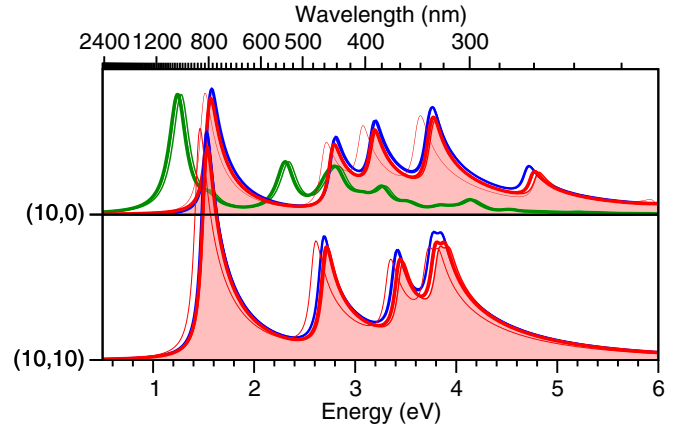


FIG. 3. Convergence of calculated optical absorbance $\text{Im}[\varepsilon(\omega)]$ spectra along the SWCNT axis in nm (upper axis) and eV (lower axis) for semiconducting (10, 0) and metallic (10, 10) SWCNTs from LCAO-TDDFT- k - ω (red) with single (SZP), double (DZP), triple (TZP), and quadruple (QZP) ζ -polarized basis sets (in order of increasing thickness), PW-TDDFT- k - ω (blue) with $E_{\text{cut}} = 340$ (thin) and 700 eV (thick), and G_0W_0 -BSE (green) with $E_{\text{cut}} = 10$ (thin), 50 (thicker), and 100 eV (thickest). Filled regions denote the DZP spectra.

calculating Δ_{QP} for a more tractable semiconducting zigzag (10, 0) SWCNT, one could then estimate the QP band gap $E_{\text{gap}}^{\text{QP}}$ for arbitrary chiralities using

$$E_{\text{gap}}^{\text{QP}} \approx \Delta_{\text{KS}} + \frac{\Delta_{\text{QP}}^{(10,0)}}{\Delta_x^{(10,0)}} \Delta_x. \quad (7)$$

It is worth noting that the reliability of (7) will depend on how wide a range of SWCNT diameters are considered.

Altogether this implies Δ_x will provide a qualitative correction to both the onset and intensities of the calculated spectra. As we will see in the following sections, this correction is essential for providing both a semiquantitative and qualitative description of optical absorption and electron energy loss spectra in the $\mathbf{q} \rightarrow 0^+$ limit.

B. Optical absorption spectra

Before comparing our LCAO-TDDFT- k - ω calculations with measured spectra, we must first consider the convergence of these calculations at a theoretical level. This is because LCAO calculations in general, and at a TDDFT level in particular, are often dependent on the choice of basis set [57].

In Fig. 3 we show the convergence of the optical absorbance spectra for the semiconducting (10, 0) and metallic (10, 10) SWCNTs with LCAO basis set for LCAO-TDDFT- k - ω [single (SZP), double (DZP), triple (TZP), and quadruple (QZP) ζ polarized] and energy cutoff for PW-TDDFT- k - ω ($E_{\text{cut}} = 340$ and 700 eV). As shown in Table I, the zigzag (10, 0) and armchair (10, 10) SWCNTs have smaller unit cell lengths but comparable diameters to the chiral SWCNTs measured in Refs. [24,25]. This makes them highly suitable for benchmarking our SWCNT calculations with LCAO-TDDFT- k - ω .

Figure 3 shows that the LCAO-TDDFT- k - ω optical absorbance spectra are already sufficiently converged with a DZP basis set, as compared to TZP and QZP calculations. However, the inclusion of other types of functions to these basis sets could still potentially alter the calculated spectra. To eliminate this possibility, we also compare with the PW-TDDFT- k - ω optical absorbance spectra, which may be systematically converged with respect to the energy cutoff E_{cut} .

As we see from Fig. 3, we already obtain converged PW-TDDFT- k - ω spectra for $E_{\text{cut}} = 340$ eV. More importantly, by comparing the optical absorbance spectra from LCAO-TDDFT- k - ω with a DZP basis set with that from PW-TDDFT- k - ω , we see the former is semiquantitatively converged with respect to the later for peak energies, intensities, and overall shape. We do notice a slight underestimation of the optical absorbance intensity with LCAO-TDDFT- k - ω , which may be attributable to the difficulty in describing unoccupied orbitals with LCAOs. However, since from hereon we will systematically normalize the calculated and measured spectra, this minor difference will not affect our results.

To determine the effect of excitonic binding on the measured spectra we have performed G_0W_0 calculations [31] of the QP electronic band gap $E_{\text{gap}}^{\text{QP}}$ and BSE calculations [32] of the optical absorption spectra for the (10, 0) SWCNT. We obtain a QP band gap of $E_{\text{gap}}^{\text{QP}} \approx 1.82$ eV, consistent with $E_{\text{gap}}^{\text{QP}} \approx 1.72$ eV from Ref. [58]. From our BSE calculations we obtain a substantial exciton binding energy for the first bright exciton of $E_{\text{bind}} = E_{\text{gap}}^{\text{QP}} - \hbar\omega_{\text{ex}} \approx 0.58$ eV, consistent with the (8, 0) SWCNT $E_{\text{bind}} \approx 0.44$ and 0.99 eV from Refs. [3,58], respectively. Taken altogether, we obtain a G_0W_0 -BSE energy for the first transition of $E_{11} \approx 1.24$ eV, in qualitative agreement with $E_{11} \approx 1.55$ eV from our LCAO-TDDFT- k - ω and PW-TDDFT- k - ω calculations.

In Fig. 3 we also directly compare our G_0W_0 -BSE, PW-TDDFT- k - ω , and LCAO-TDDFT- k - ω calculated optical absorption spectra. We find the relative intensity, peak separation, and overall shape of the spectra are in qualitative agreement between the three methods. Although we find the G_0W_0 -BSE spectra are redshifted by about 0.3 eV relative to the PW-TDDFT- k - ω and LCAO-TDDFT- k - ω spectra, this difference may be attributed to the inclusion of exciton binding at the G_0W_0 -BSE level.

It should be noted that the derivative discontinuity correction Δ_x to the KS band gap Δ_{KS} is of “first order,” with QP G_0W_0 [31], partially self-consistent (scQPGW₀) [51], and fully self-consistent (scQPGW) [59,60] QP methods each generally blueshifting the electronic band gap further [36,37]. For example, employing scQPGW₀ to obtain $E_{\text{gap}}^{\text{QP}}$ for the (10, 0) SWCNT blueshifts the G_0W_0 -BSE spectra by 0.08 eV, yielding $E_{11} \approx 1.32$ eV, in better agreement with our LCAO-TDDFT- k - ω results. This suggests, while $E_{\text{gap}} = \Delta_{\text{KS}} + \Delta_x$ underestimates the QP band gap $E_{\text{gap}}^{\text{QP}} = \Delta_{\text{KS}} + \Delta_{\text{QP}}$, the excitonic binding energy E_{bind} redshifts the BSE spectra a commensurate amount, resulting in a fortuitous error cancellation in our LCAO-TDDFT- k - ω calculations.

In general, the excitonic binding energy E_{bind} is constrained by a material’s ability to screen the electron-hole pair, i.e., ϵ_{∞} . This suggests a direct linear relationship should exist between ϵ_{∞}^{-1} and E_{bind} . Since we have already shown ϵ_{∞}^{-1} is directly

proportional to Δ_x in Fig. 2, we may model the excitonic binding energy using

$$E_{\text{bind}} \approx \frac{E_{\text{bind}}^{(10,0)}}{\Delta_x^{(10,0)}} \Delta_x. \quad (8)$$

From (7) and (8) we may derive a simple linear model for the QP E_{11} transition energy in terms of Δ_x ,

$$E_{11} \approx \Delta_{\text{KS}} + \frac{\Delta_{\text{QP}}^{(10,0)} - E_{\text{bind}}^{(10,0)}}{\Delta_x^{(10,0)}} \Delta_x. \quad (9)$$

Employing the scQPGW₀ energy shift $\Delta_{\text{QP}}^{(10,0)} \approx 1.138$ eV in (7), we find $E_{\text{gap}}^{\text{QP}} \approx \Delta_{\text{KS}} + 1.444\Delta_x$, reflecting a systematic blueshifting of the QP electronic band gap. Likewise, employing the BSE excitonic binding energy $E_{\text{bind}}^{(10,0)} \approx 0.58$ eV in (8), we find $E_{\text{bind}} \approx 0.736\Delta_x$. Combining these results in (9), we find $E_{11} \approx \Delta_{\text{KS}} + 0.708\Delta_x \approx \Delta_{\text{KS}} + 1.7\epsilon_{\infty}^{-1}$, reflecting the fact that our LCAO-TDDFT- k - ω calculations somewhat overestimate the scQPGW₀-BSE E_{11} transition energy. This demonstrates how essential it is to also benchmark our theoretical calculations with experimental measurements.

In Fig. 4 we directly compare the optical absorption spectra calculated with our LCAO-TDDFT- k - ω code to the experimental data provided in Ref. [24]. The experimental data were normalized, that is, the highest value was set to 1.5 in arbitrary units. Likewise, we normalized the maximum of the calculated spectra to 1 in the same arbitrary units.

In each of the optical absorption spectra, the first peak corresponds to the first excitation associated with van Hove singularities, i.e., the E_{11} transition. The second highest peak corresponds to the second excitation of this kind, E_{22} . We were able to resolve in some cases a peak between these two, such as in the (9, 4), (9, 1), (8, 3), (7, 5), and (9, 4). We can also observe excitations higher in energy than the E_{22} , which are typically redshifted by about 0.3 eV relative to the experimental peaks. From hereon, we shall restrict our discussion to the E_{11} and the E_{22} excitations.

All spectra were calculated using the derivative discontinuity correction of the exchange part of the GLLB-SC functional Δ_x from Eq. (1). As seen in Eq. (2), this not only shifts the KS eigenenergies, yielding a good description of the first excitation energy E_{11} or the band gap E_{gap} , but also changes the intensities of all the transitions.

For all the SWCNTs studied herein, we obtained a semiquantitative agreement in the description of the relative intensities and positions of the E_{11} and E_{22} transitions. We find that the E_{11} transition is more intense than the E_{22} , except in the case of the (9, 1) SWCNT. The first transition being more intense than the second transition is a feature also observed in the experimental data.

When comparing the spectra of all the SWCNTs, we find that the energies of the E_{22} transitions are uncorrelated to those of the E_{11} transitions. The energies of these two transitions are neither separated by the same amount nor is one proportional to the other. In some cases they are closer than in others. Although the E_{11} and the E_{22} transitions are uncorrelated, the spectra calculated with the LCAO-TDDFT- k - ω code are able to reproduce semiquantitatively the values of both these transitions’ energies.

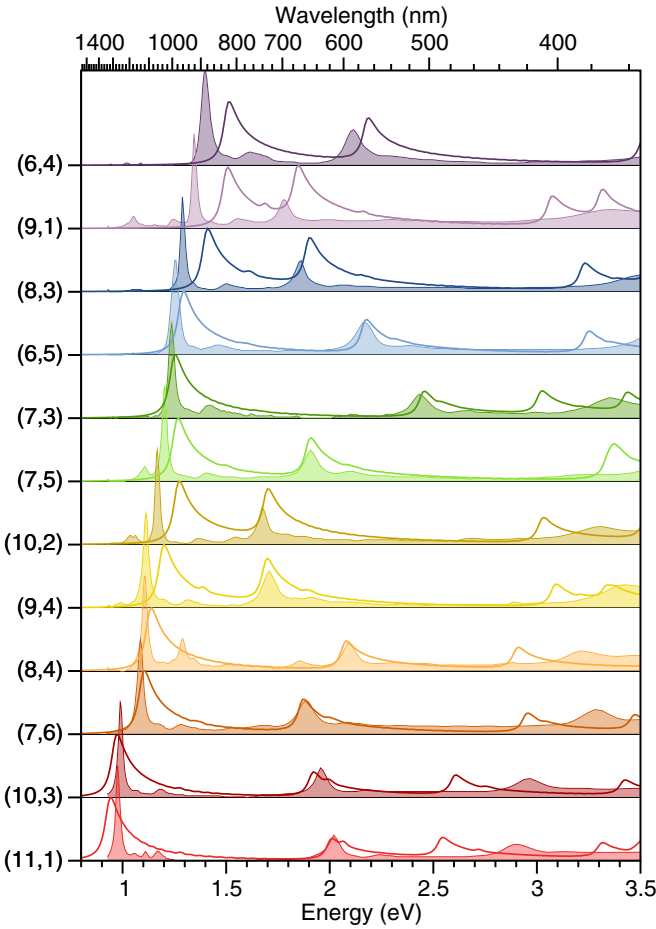


FIG. 4. Comparison of LCAO-TDDFT- k - ω calculated (solid lines) and measured (filled regions, Ref. [24]) optical absorbance $\text{Im}[\epsilon(\omega)]$ spectra along the SWCNT axis in nm (upper axis) and eV (lower axis) for chirality sorted (6, 4), (9, 1), (8, 3), (6, 5), (7, 3), (7, 5), (10, 2), (9, 4), (8, 4), (7, 6), (10, 3), and (11, 1) SWCNTs shown in Fig. 1.

The optical absorption spectra shown in Fig. 4 corresponds to the first 12 SWCNTs listed in Table I, which vary widely in length and number of atoms per unit cell. We can observe that the spectra calculated using the LCAO-TDDFT- k - ω code reproduce the features of the experimental data of these very different SWCNTs, showing that it is surprisingly robust when calculating the optical absorbance of carbon-based 1D nanostructures.

In order to calculate the optical absorption spectra of SWCNTs with large unit cells, it was also necessary to implement both domain decomposition of the real space grids and parallelization with respect to k points. This type of parallelization proved essential for allowing us to perform distributed memory calculations with limited computational resources.

C. E_{11} and E_{22} transitions

In Fig. 5(a) we directly compare the measured E_{11} transition energies from optical absorption and electron loss spectroscopy of Refs. [24,25], respectively, with our LCAO-TDDFT- k - ω calculated values. We also compare the values

obtained with the derivative discontinuity correction of the exchange part of the GLLB-SC functional Δ_x and without this correction, that is, using only the PBEsol xc functional.

The PBEsol functional yields an estimation of the band gap with an average error of $\epsilon \approx -0.30 \pm 0.02$ eV. Although it reproduces the trend better than in the case of the GLLB-SC functional, the band gap is always significantly underestimated. When we add the derivative discontinuity correction of the GLLB-SC functional, the average error is $\epsilon \approx 0 \pm 0.07$ eV, that is, much smaller than when not adding the correction and well within the expected 0.1 eV accuracy of DFT calculations. Nevertheless, the standard deviation is somewhat larger. This shows that it is important to use the derivative discontinuity correction of the GLLB-SC functional to properly describe the electronic structure and have a better agreement with the experimentally measured spectra onset for SWCNTs.

In Fig. 5(b) we directly compare the measured E_{22} transition energies from optical absorption spectroscopy [24] with our LCAO-TDDFT- k - ω calculated values including the derivative discontinuity correction of the GLLB-SC functional Δ_x . Here we obtain a similar agreement to that for the E_{11} transition, with an average error of $\epsilon \approx 26 \pm 33$ meV. This is again well within the expected 0.1 eV accuracy of DFT calculations. It is important to note that the E_{11} and E_{22} transition energies are almost completely uncorrelated, as shown in Fig. 5, so that the near quantitative agreement we obtain is rather independent and systematic.

To demonstrate whether our neglect of excitonic binding in our LCAO-TDDFT- k - ω calculations is sufficiently compensated for by our underestimation of the QP band gap $E_{\text{gap}}^{\text{QP}}$, in Fig. 6 we compare measured E_{11} transition energies [24,25] with our scQPGW₀-BSE models $E_{11} \approx \Delta_{\text{KS}} + 0.708\Delta_x \approx \Delta_{\text{KS}} + 1.7\epsilon_{\infty}^{-1}$. Both models yield a semiquantitative description of the E_{11} transition energies, with an overall average error of $\epsilon \approx -59 \pm 50$ meV. This is well within the expected 0.1 eV accuracy of G_0W_0 -BSE calculations. These results provide further independent corroboration of the reliability of our LCAO-TDDFT- k - ω calculations for describing the optical absorption spectra of SWCNTs.

Based on the results of this subsection and the previous one, we have shown that the LCAO-TDDFT- k - ω code can reproduce with great accuracy the uncorrelated E_{11} and E_{22} transition energies for SWCNTs. Moreover, the fact that we are obtaining such a good agreement suggests that we are considering the most relevant processes that are taking place during the optical absorption. This also suggests that transitions that include charge transfer, which are not described by our method, do not occur in these SWCNTs.

D. Electron energy loss spectroscopy

So far we have considered the optical absorption spectra calculated using the LCAO-TDDFT- k - ω code, defined as the imaginary part of the dielectric function $\text{Im}[\epsilon(\omega)]$, for semiconducting SWCNTs. Now we will consider the electron energy loss spectroscopy of both metallic and semiconducting SWCNTs, provided in Ref. [25]. In so doing we are able to also assess the accuracy of the real part of the dielectric function $\text{Re}[\epsilon(\omega)]$. This is because the electron energy loss spectra is the negative of the imaginary part of the inverse

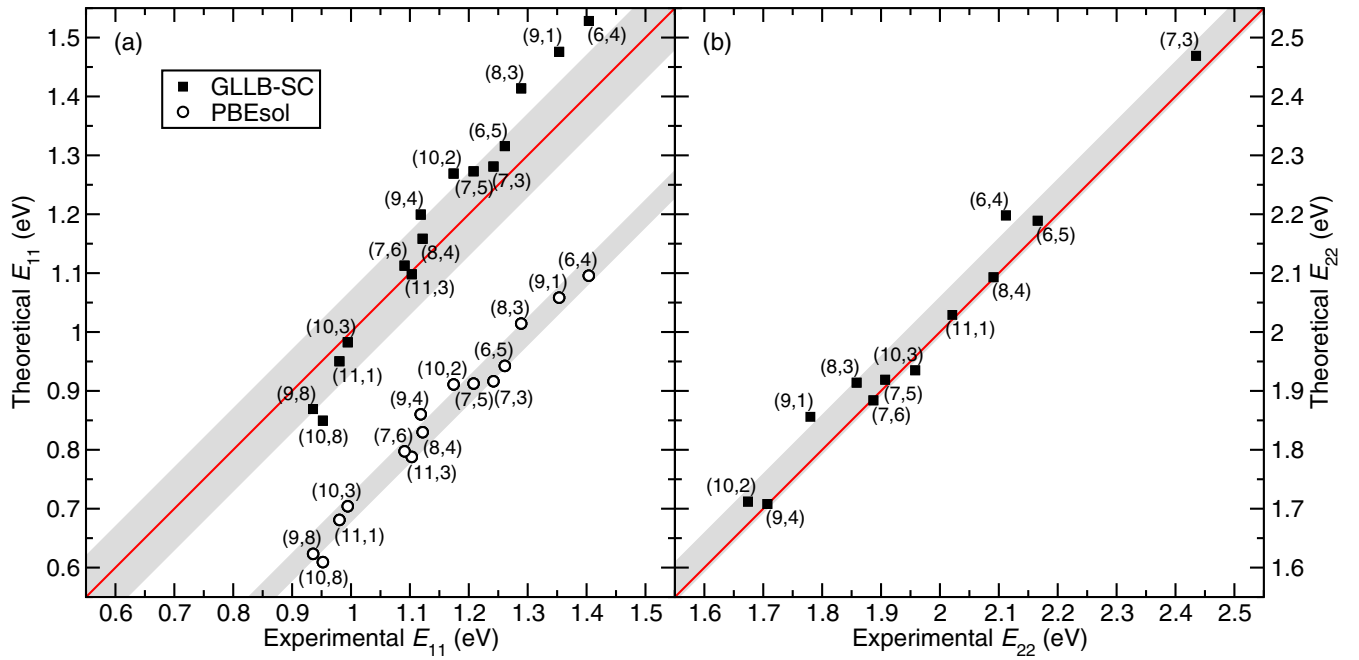


FIG. 5. Theoretical versus experimental (a) E_{11} and (b) E_{22} transition energies in eV from LCAO-TDDFT- k - ω including (GLLB-SC [29], filled squares) and neglecting (PBEsol [49], open circles) the derivative discontinuity correction Δ_x and from optical absorbance and electron energy loss measurements of Refs. [24,25], respectively, for 15 different SWCNT chiralities. The average errors for GLLB-SC (a) E_{11} ($\epsilon \approx 0 \pm 70$ meV) and (b) E_{22} ($\epsilon \approx 20 \pm 33$ meV) transitions and for PBEsol (a) E_{11} ($\epsilon \approx -300 \pm 3$ meV) transitions are shown as gray regions. Red lines are provided to guide the eye.

of the dielectric function $-\text{Im}[\epsilon^{-1}(\omega)]$, i.e., $\frac{\text{Im}[\epsilon(\omega)]}{\text{Re}[\epsilon(\omega)]^2 + \text{Im}[\epsilon(\omega)]^2}$. In this way we are further assessing the robustness of the LCAO-TDDFT- k - ω code by considering another of its out-

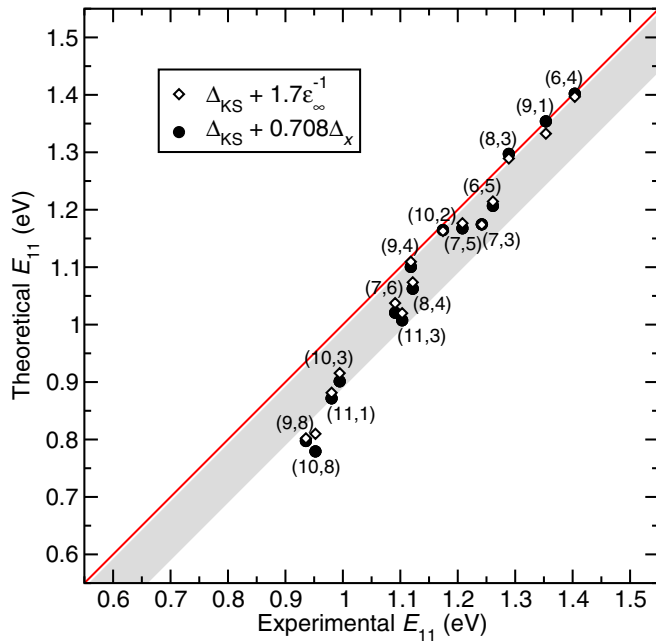


FIG. 6. Theoretical versus experimental E_{11} transition energies in eV of $E_{11} \approx \Delta_{KS} + 0.708\Delta_x$ (black circles) and $E_{11} \approx \Delta_{KS} + 1.7\epsilon_\infty^{-1}$ (white diamonds) and optical absorbance and electron energy loss measurements of Refs. [24,25], respectively, for 15 different SWCNT chiralities. Average error $\epsilon \approx -59 \pm 50$ meV shown as gray regions and red line provided to guide the eye.

puts. Furthermore, the comparison will be done with respect to measured spectra that correspond to different experiments than those used in the previous sections.

In Fig. 7(a) we compare the electron energy loss spectra of semiconducting SWCNTs measured in Ref. [25] with our calculations using the LCAO-TDDFT- k - ω code. We find for all five semiconducting SWCNTs that the first and second peaks are somewhat blueshifted with respect to the measured spectra by about 0.2 and 0.4 eV on average, respectively. These peaks are assigned the E_{11} and E_{22} interband transitions.

Above these two peaks in energy there is a trough and one, two, or three intermediate peaks before a broader and last peak in the measured spectra. The third of all the peaks, that is, the first of the intermediate peaks or the one right after the trough, is always redshifted with respect to the measured spectra by about 0.37 eV on average. These intermediate peaks correspond to the E_{33} , E_{44} , and E_{55} interband transitions which can be easily identified in the spectra of the (10, 8) and the (9, 8) SWCNTs.

The broader and higher energy peak is blueshifted by about 0.29 eV on average, and is the well-known π plasmon of SWCNTs [61–63]. The spectra have the same behavior in general up to an energy shift, but in the spectra of the (8, 4) and the (8, 3) SWCNTs the peaks are closer together and harder to recognize. As in the experimental results, the spectra present a monotonic downshift as the diameter of the SWCNT increases.

Turning to an analysis of the metallic SWCNTs' electron energy loss spectroscopy in Fig. 7(b), we observe a strong peak at around 1 eV (marked with an *) that also matches what is observed in the experimental spectra. These peaks, which are present only in the spectra of metallic SWCNTs,

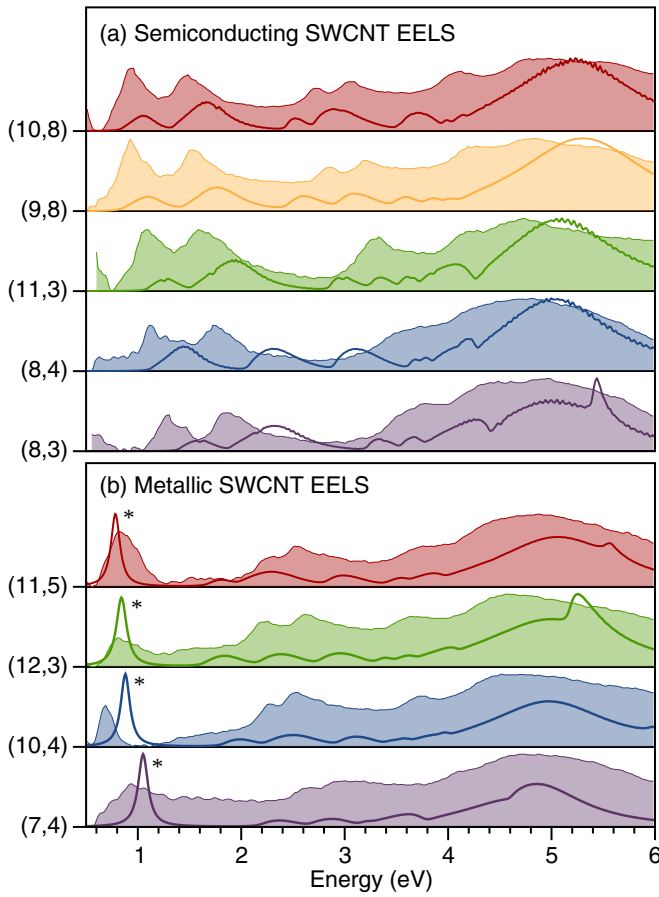


FIG. 7. Comparison of LCAO-TDDFT- k - ω calculated (solid lines) and measured (filled regions, Ref. [25]) electron energy loss $-\text{Im}[\epsilon^{-1}(\omega)]$ spectra along the SWCNT axis in eV for chirality sorted (a) semiconducting (10, 8), (9, 8), (11, 3), (8, 4), and (8, 3) and (b) metallic (11, 5), (12, 3), (10, 4) and (7, 4) SWCNTs shown in Fig. 1, with Drude intraband plasmons ω_P (*) marked.

correspond to free charge carrier Drude plasmons ω_P . In other words, an intraband excitation that causes quantized collective oscillations of electrons.

Going higher in energy, there is a trough and three well-known peaks. The first two of these peaks correspond to M_{11} (E_{11}) transitions. The splitting of the transition into two peaks is probably caused by the trigonal wrapping effect [25]. The third peak corresponds to the M_{22} transition. All of these transitions can be compared to peaks in the experimental data, although they are redshifted by about 0.15 eV. Finally, the broader and higher energy peak is again blueshifted by about 0.28 eV, and is the well-known π plasmon of SWCNTs [61–63]. We also observe intense peaks in the spectra above 5 eV of the (11, 5) and (12, 3) SWCNTs, which could be related to splitting of the π plasmon.

In summary, we obtained an accurate energy for the plasmonic transition and also a qualitative description of the two peaks related to the M_{11} transition and the peak related to the M_{22} up to a redshift. In this way we have assessed both the real and imaginary part of the dielectric function calculated using the LCAO-TDDFT- k - ω code and found it provides a

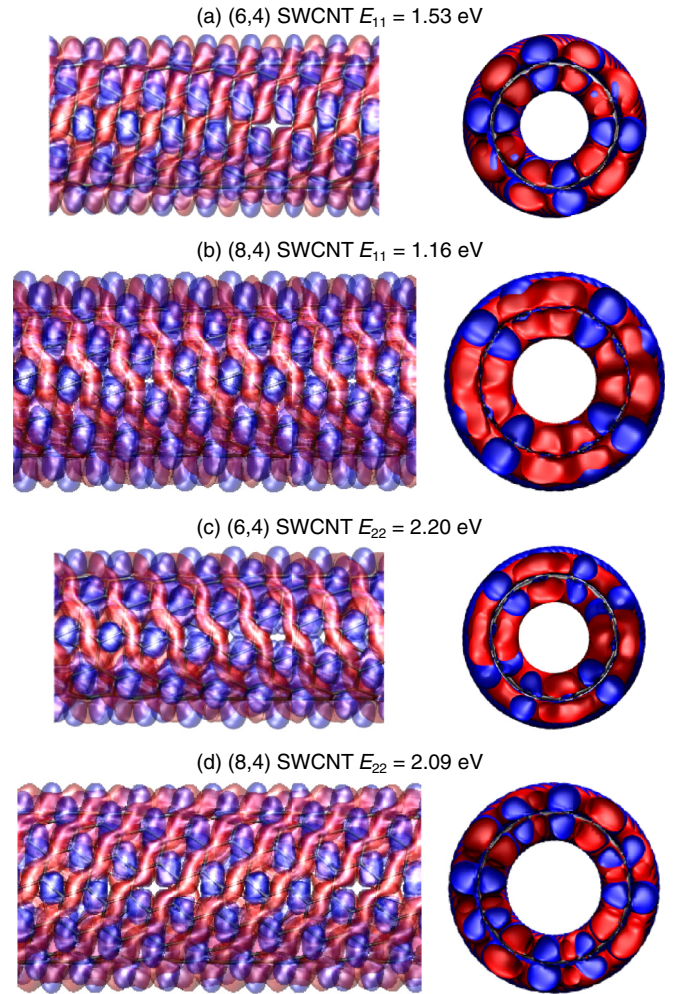


FIG. 8. Electron-hole density difference $\Delta\rho(\mathbf{r}, \omega) = \rho_e(\mathbf{r}, \omega) + \rho_h(\mathbf{r}, \omega)$ positive (red) and negative (blue) isosurfaces for the (a) and (b) E_{11} and (c) and (d) E_{22} transitions of the (a) and (c) (6, 4) ($E_{11} \approx 1.53$, $E_{22} \approx 2.20$ eV) and (b) and (d) (8, 4) ($E_{11} \approx 1.16$, $E_{22} \approx 2.20$ eV) semiconducting SWCNTs along the axis (left) and in the plane (right) of the nanotube.

robust and efficient method for modeling electron energy loss spectra.

E. Electron-hole density difference

Having demonstrated the reliability of our LCAO-TDDFT- k - ω code for describing both the optical absorption and electron energy loss spectra of SWCNTs in the previous sections, we may now use the electron-hole density difference $\Delta\rho(\mathbf{r}, \omega)$, calculated from Eq. (5), to model the spatial distribution of the most relevant bright excitons. In so doing, we may probe the spatially resolved optical absorption and electron energy loss spectroscopy of SWCNTs, and their underlying physical makeup.

In Fig. 8 we show the spatially resolved electron-hole density difference $\Delta\rho(\mathbf{r}, \omega)$ of the E_{11} and E_{22} transitions for two semiconducting SWCNTs with quite different transition energies. Regions of negative charge (blue) correspond to

the excited electron, whereas regions of positive charge (red) correspond to the hole. For both the E_{11} and E_{22} transitions we find that the positive (or hole) density is distributed in a continuous spiral around the nanotube, whereas the negative (or electron) density follows the same pattern but is discontinuous. This suggests the hole density corresponds to bonding orbitals wrapping the SWCNT, whereas the electron density corresponds to antibonding orbitals localized on individual C–C bonds.

In fact, the plots in Fig. 8 in the SWCNT's plane show the electron-hole density difference isosurfaces are composed of π orbitals, with a nodal plane on the SWCNT's surface. These results clearly demonstrate that both the E_{11} and E_{22} transitions are indeed $\pi \rightarrow \pi$ transitions, as expected.

It is interesting to note that the spatial distribution of the E_{11} transition of the (6, 4) SWCNT more closely resembles that of the E_{22} transition of the (8, 4) SWCNT, whereas the E_{22} transition of the (6, 4) SWCNT more closely resembles that of the E_{11} transition of the (8, 4) SWCNT. This is evident from both the direction of the wrapping of the positive hole distributions around the nanotube axis and the slice in the nanotube plane. This clearly suggests the spatial distribution of the individual excitonic peaks is highly dependent on the SWCNT's chirality, and not simply a function of the peak's energy.

In Fig. 9 we show the spatially resolved electron-hole density difference $\Delta\rho(\mathbf{r}, \omega)$ of the Drude intraband plasmon ω_p for three different metallic SWCNTs. Again, regions of negative charge (blue) correspond to the excited electron, whereas regions of positive charge (red) correspond to the hole. In contrast to the E_{11} and E_{22} transitions of the semiconducting SWCNTs (cf. Fig. 8), we find for each of the three metallic nanotubes the plasmon excitation has negative (or electron) density distributed in a continuous spiral around the nanotube, whereas the positive (or hole) density follows the same pattern but is discontinuous. This suggests the electron density corresponds to bonding orbitals wrapping the SWCNT, whereas the hole density corresponds to antibonding orbitals localized on individual C–C bonds.

As was the case for the semiconducting E_{11} and E_{22} transitions (cf. Fig. 8), the plots in Fig. 9 in the SWCNT's plane show the electron-hole density difference isosurfaces for the Drude intraband plasmons ω_p are also composed of π orbitals, with a nodal plane on the SWCNT's surface. These results clearly demonstrate that the Drude plasmon is also composed of $\pi \rightarrow \pi$ transitions, as expected. However, the nearly continuous excited electron's density seems to be a property of this metallic plasmon.

Overall, these results provide us with added insight into the physical makeup of the experimentally observed peaks in optical absorbance and electron energy loss spectra. This information has the potential of further optimizing a SWCNT's overlap with donor molecules when designing organic photovoltaic cells.

IV. CONCLUSIONS

We have performed an in-depth analysis of the optical absorption and electron energy loss spectra of SWCNTs, 1D structures with properties determined by their (m, n)

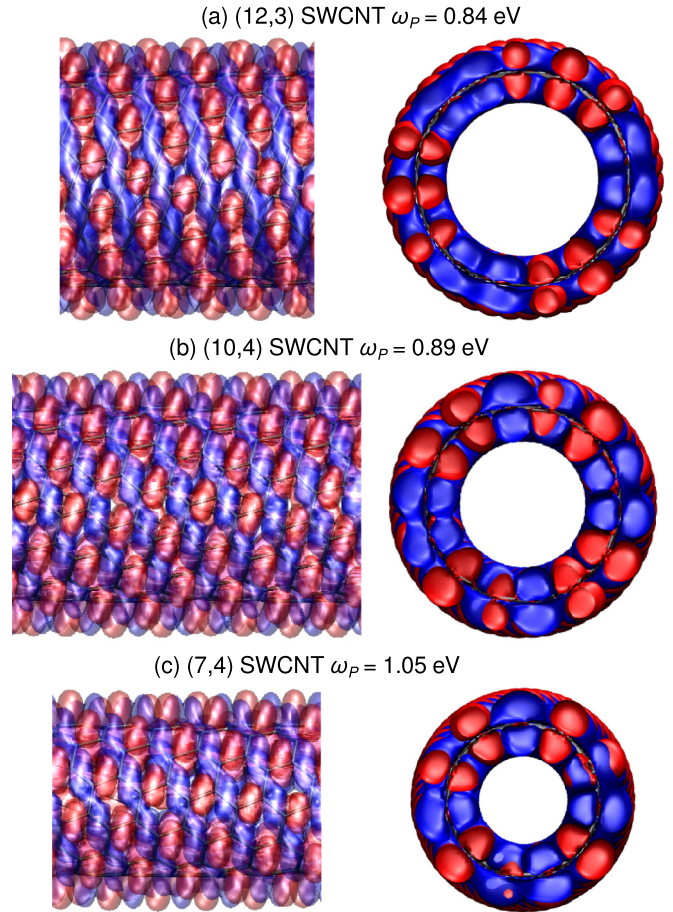


FIG. 9. Electron-hole density difference $\Delta\rho(\mathbf{r}, \omega) = \rho_e(\mathbf{r}, \omega) + \rho_h(\mathbf{r}, \omega)$ positive (red) and negative (blue) isosurfaces for the plasmon excitations ω_p of the (a) (12, 3) ($\omega_p \approx 0.84$ eV), (b) (10, 4) ($\omega_p \approx 0.89$ eV), and (c) (7, 4) ($\omega_p \approx 1.05$ eV) metallic SWCNTs along the axis (left) and in the plane (right) of the nanotube.

chiral indices. We have considered a variety of SWCNTs with different indices and found that our theoretical optical absorption spectra, given by the imaginary part of the dielectric function, agree semiquantitatively with both our more computationally demanding PW-TDDFT- k - ω , G_0W_0 -BSE, and scQPGW₀ calculations and the experimental data when the derivative discontinuity correction of the GLLB-SC functional Δ_x is employed in our LCAO-TDDFT- k - ω code. We also see that both the calculated E_{11} and E_{22} transition energies have an average error much smaller than the expected accuracy of DFT calculations, with the E_{22} transition energies having an even better agreement than the E_{11} . This result is rather surprising since the E_{11} and E_{22} energies are uncorrelated. Furthermore, we assessed the real part of the dielectric function by comparing our calculated electron energy loss spectra, given by minus the imaginary part of the inverse dielectric function, to experimental data. We were able to reproduce the qualitative behavior of the spectra and to obtain an accurate energy for the Drude intraband plasmon peak ω_p in metallic SWCNTs. Finally, we have employed the electron-hole density difference $\Delta\rho(\mathbf{r}, \omega)$ to model the spatial distribution of the excitons. We find, as expected, the E_{11} and

E_{22} transitions in semiconducting SWCNTs and the Drude intraband plasmon ω_p in metallic SWCNTs all involve π levels which wrap around the SWCNTs. Altogether, these results demonstrate the surprising reliability and efficiency of a simplified LCAO-based TDDFT calculation in the optical limit for describing the optical absorbance and electron energy loss spectra of carbon-based macromolecules. This work blazes the trail towards the computational design of

complex carbon-based macromolecular organic photovoltaic systems *in silico*.

ACKNOWLEDGMENTS

This work employed the Imbabura cluster of Yachay Tech University, which was purchased under Contract No. 2017-024 (SIE-UIITEY-007-2017).

-
- [1] R. H. Baughman, A. A. Zakhidov, and W. A. de Heer, Carbon nanotubes—the route toward applications, *Science* **297**, 787 (2002).
- [2] M. S. Dresselhaus, G. Dresselhaus, and P. Avouris (Eds.), *Carbon Nanotubes: Synthesis, Structure, Properties, and Applications* (Springer, Berlin, 2001).
- [3] C. D. Spataru, S. Ismail-Beigi, L. X. Benedict, and S. G. Louie, Excitonic Effects and Optical Spectra of Single-Walled Carbon Nanotubes, *Phys. Rev. Lett.* **92**, 077402 (2004).
- [4] H. Kataura, Y. Kumazawa, Y. Maniwa, I. Umezū, S. Suzuki, Y. Ohtsuka, and Y. Achiba, Optical properties of single-wall carbon nanotubes, *Syn. Metals* **103**, 2555 (1999).
- [5] T. Yamamoto, K. Watanabe, and E. R. Hernández, Mechanical properties, thermal stability and heat transport in carbon nanotubes, in *Carbon Nanotubes: Advanced Topics in the Synthesis, Structure, Properties and Applications*, edited by A. Jorio, G. Dresselhaus, and M. S. Dresselhaus (Springer, Berlin, 2008), pp. 165–195.
- [6] K. M. Liew, C. H. Wong, X. Q. He, and M. J. Tan, Thermal stability of single and multi-walled carbon nanotubes, *Phys. Rev. B* **71**, 075424 (2005).
- [7] W. Liang, M. Bockrath, D. Bozovic, J. H. Hafner, M. Tinkham, and H. Park, Fabry-Perot interference in a nanotube electron waveguide, *Nature (London)* **411**, 665 (2001).
- [8] S. Frank, P. Poncharal, Z. Wang, and W. A. De Heer, Carbon nanotube quantum resistors, *Science* **280**, 1744 (1998).
- [9] E. Kymakis and G. Amaratunga, Single-wall carbon nanotube/conjugated polymer photovoltaic devices, *Appl. Phys. Lett.* **80**, 112 (2002).
- [10] E. Kymakis, E. Koudoumas, I. Franghiadakis, and G. Amaratunga, Post-fabrication annealing effects in polymer-nanotube photovoltaic cells, *J. Phys. D Appl. Phys.* **39**, 1058 (2006).
- [11] S. Campidelli, B. Ballesteros, A. Filoramo, D. Díaz, G. de la Torre, T. Torres, G. A. Rahman, C. Ehli, D. Kiessling, and F. Werner, Facile decoration of functionalized single-wall carbon nanotubes with phthalocyanines via “click chemistry”, *J. Am. Chem. Soc.* **130**, 11503 (2008).
- [12] J. Bartelmess, B. Ballesteros, G. de la Torre, D. Kiessling, S. Campidelli, M. Prato, T. Torres, and D. M. Guldi, Phthalocyanine-pyrene conjugates: A powerful approach toward carbon nanotube solar cells, *J. Am. Chem. Soc.* **132**, 16202 (2010).
- [13] D. M. Guldi, G. Rahman, M. Prato, N. Jux, S. Qin, and W. Ford, Single-wall carbon nanotubes as integrative building blocks for solar-energy conversion, *Angew. Chem. Int. Ed.* **44**, 2015 (2005).
- [14] M.-H. Ham, J. H. Choi, A. A. Boghossian, E. S. Jeng, R. A. Graff, D. A. Heller, A. C. Chang, A. Mattis, T. H. Bayburt, Y. V. Grinkova, A. S. Zeiger, K. J. V. Vliet, E. K. Hobbie, S. G. Sligar, C. A. Wraight, and M. S. Strano, Photoelectrochemical complexes for solar energy conversion that chemically and autonomously regenerate, *Nat. Chem.* **2**, 929 (2010).
- [15] C. Zamora-Ledezma, C. Blanc, and E. Anglaret, Orientational order of single-wall carbon nanotubes in stretch-aligned photoluminescent composite films, *Phys. Rev. B* **80**, 113407 (2009).
- [16] F. J. Torres-Canas, C. Blanc, C. Zamora-Ledezma, P. Silva, and E. Anglaret, Dispersion and individualization of SWNT in surfactant-free suspensions and composites of hydrosoluble polymers, *J. Phys. Chem. C* **119**, 703 (2014).
- [17] R. B. Weisman and J. Kono, Introduction to optical spectroscopy of single-wall carbon nanotubes, in *Handbook of Carbon Nanomaterials* (World Scientific, Singapore, 2019), pp. 1–43.
- [18] A. Zangwill, A half century of density functional theory, *Phys. Today* **68**, 34 (2015).
- [19] J. K. Nørskov, T. Bligaard, J. Rossmeisl, and C. H. Christensen, Towards the computational design of solid catalysts, *Nat. Chem.* **1**, 37 (2009).
- [20] A. Jain, S. P. Ong, G. Hautier, W. Chen, W. D. Richards, S. Dacek, S. Cholia, D. Gunter, D. Skinner, G. Ceder, and K. A. Persson, Commentary: The materials project: A materials genome approach to accelerating materials innovation, *APL Mater.* **1**, 011002 (2013).
- [21] L. N. Glanzmann, D. J. Mowbray, D. G. Figueroa del Valle, F. Scotognella, G. Lanzani, and A. Rubio, Photoinduced absorption within single-walled carbon nanotube systems, *J. Phys. Chem. C* **120**, 1926 (2015).
- [22] L. N. Glanzmann and D. J. Mowbray, Theoretical insight into the internal quantum efficiencies of polymer/C60 and polymer/SWNT photovoltaic devices, *J. Phys. Chem. C* **120**, 6336 (2016).
- [23] R. B. Weisman and S. Subramoney, Carbon nanotubes, *Electrochem. Soc. Interface* **15**, 42 (2006).
- [24] X. Wei, T. Tanaka, Y. Yomogida, N. Sato, R. Saito, and H. Kataura, Experimental determination of excitonic band structures of single-walled carbon nanotubes using circular dichroism spectra, *Nat. Commun.* **7**, 12899 (2016).
- [25] R. Senga, T. Pichler, and K. Suenaga, Electron spectroscopy of single quantum objects to directly correlate the local structure to their electronic transport and optical properties, *Nano Lett.* **16**, 3661 (2016).

- [26] K. Lyon, M. R. Preciado-Rivas, D. J. Mowbray, and V. Despoja, LCAO-TDDFT- k - ω : Spectroscopy in the optical limit, [arXiv:1909.13409](https://arxiv.org/abs/1909.13409).
- [27] M. R. Preciado-Rivas, D. J. Mowbray, K. Lyon, A. H. Larsen, and B. F. Milne, Optical excitations of chlorophyll *a* and *b* monomers and dimers, *J. Chem. Phys.* **151**, 174102 (2019).
- [28] The LCAO-TDDFT- k - ω code is available free of charge from github.com/lcao-tddft-k-omega/lcao-tddft-k-omega.
- [29] M. Kuisma, J. Ojanen, J. Enkovaara, and T. T. Rantala, Kohn-Sham potential with discontinuity for band gap materials, *Phys. Rev. B* **82**, 115106 (2010).
- [30] J. Enkovaara, C. Rostgaard, J. J. Mortensen, J. Chen, M. Duřak, L. Ferrighi, J. Gavnholt, C. Glinsvad, V. Haikola, H. A. Hansen, H. H. Kristoffersen, M. Kuisma, A. H. Larsen, L. Lehtovaara, M. Ljungberg, O. Lopez-Acevedo, P. G. Moses, J. Ojanen, T. Olsen, V. Petzold, N. A. Romero *et al.*, Electronic structure calculations with GPAW: A real-space implementation of the projector augmented-wave method, *J. Phys.: Condens. Matter* **22**, 253202 (2010).
- [31] L. Hedin, New method for calculating the one-particle Green's function with application to the electron-gas problem, *Phys. Rev.* **139**, A796 (1965).
- [32] E. E. Salpeter and H. A. Bethe, A relativistic equation for bound-state problems, *Phys. Rev.* **84**, 1232 (1951).
- [33] F. Tran and P. Blaha, Importance of the kinetic energy density for band gap calculations in solids with density functional theory, *J. Phys. Chem. A* **121**, 3318 (2017).
- [34] J. Heyd, G. E. Scuseria, and M. Ernzerhof, Hybrid functionals based on a screened Coulomb potential, *J. Chem. Phys.* **118**, 8207 (2003).
- [35] G. Onida, L. Reining, and A. Rubio, Electronic excitations: Density-functional versus many-body Green's-function approaches, *Rev. Mod. Phys.* **74**, 601 (2002).
- [36] A. Migani, D. J. Mowbray, A. Iacomino, J. Zhao, H. Petek, and A. Rubio, Level alignment of a prototypical photocatalytic system: Methanol on TiO₂(110), *J. Am. Chem. Soc.* **135**, 11429 (2013).
- [37] A. Migani, D. J. Mowbray, J. Zhao, H. Petek, and A. Rubio, Quasiparticle level alignment for photocatalytic interfaces, *J. Chem. Theory Comput.* **10**, 2103 (2014).
- [38] A. Migani, D. J. Mowbray, J. Zhao, and H. Petek, Quasiparticle interfacial level alignment of highly hybridized frontier levels: H₂O on TiO₂(110), *J. Chem. Theory Comput.* **11**, 239 (2015).
- [39] F. Tran, S. Ehsan, and P. Blaha, Assessment of the GLLB-SC potential for solid-state properties and attempts for improvement, *Phys. Rev. Mater.* **2**, 023802 (2018).
- [40] O. Gritsenko, R. van Leeuwen, E. van Lenthe, and E. J. Baerends, Self-consistent approximation to the Kohn-Sham exchange potential, *Phys. Rev. A* **51**, 1944 (1995).
- [41] O. V. Gritsenko, R. van Leeuwen, and E. J. Baerends, Direct approximation of the long- and short-range components of the exchange-correlation Kohn-Sham potential, *Int. J. Quantum Chem.* **61**, 231 (1997).
- [42] I. E. Castelli, T. Olsen, S. Datta, D. D. Landis, S. Dahl, K. S. Thygesen, and K. W. Jacobsen, Computational screening of perovskite metal oxides for optimal solar light capture, *Energy Environ. Sci.* **5**, 5814 (2012).
- [43] L. N. Glanzmann, D. J. Mowbray, and A. Rubio, PFO-BPY solubilizers for SWNTs: Modelling polymers from oligomers, *Phys. Status Solidi B* **251**, 2407 (2014).
- [44] D. J. Mowbray and A. Migani, Optical absorption spectra and excitons of dye-substrate interfaces: Catechol on TiO₂(110), *J. Chem. Theory Comput.* **12**, 2843 (2016).
- [45] J. J. Mortensen, L. B. Hansen, and K. W. Jacobsen, Real-space grid implementation of the projector augmented wave method, *Phys. Rev. B* **71**, 035109 (2005).
- [46] P. E. Blöchl, Projector augmented-wave method, *Phys. Rev. B* **50**, 17953 (1994).
- [47] S. R. Bahn and K. W. Jacobsen, An object-oriented scripting interface to a legacy electronic structure code, *Comput. Sci. Eng.* **4**, 56 (2002).
- [48] A. H. Larsen, J. J. Mortensen, J. Blomqvist, I. E. Castelli, R. Christensen, M. Duřak, J. Friis, M. N. Groves, B. Hammer, C. Hargus, E. D. Hermes, P. C. Jennings, P. B. Jensen, J. Kermode, J. R. Kitchin, E. L. Kolsbjerg, J. Kubal, K. Kaasbjerg, S. Lysgaard, J. B. Maronsson, T. Maxson *et al.*, The atomic simulation environment—a python library for working with atoms, *J. Phys.: Condens. Matter* **29**, 273002 (2017).
- [49] J. P. Perdew, A. Ruzsinszky, G. I. Csonka, O. A. Vydrov, G. E. Scuseria, L. A. Constantin, X. Zhou, and K. Burke, Restoring the Density-Gradient Expansion for Exchange in Solids and Surfaces, *Phys. Rev. Lett.* **100**, 136406 (2008).
- [50] A. H. Larsen, M. Vanin, J. J. Mortensen, K. S. Thygesen, and K. W. Jacobsen, Localized atomic basis set in the projector augmented wave method, *Phys. Rev. B* **80**, 195112 (2009).
- [51] M. Shishkin and G. Kresse, Self-consistent *GW* calculations for semiconductors and insulators, *Phys. Rev. B* **75**, 235102 (2007).
- [52] F. Hüser, T. Olsen, and K. S. Thygesen, Quasiparticle *GW* calculations for solids, molecules, and two-dimensional materials, *Phys. Rev. B* **87**, 235132 (2013).
- [53] R. W. Godby and R. J. Needs, Metal-Insulator Transition in Kohn-Sham Theory and Quasiparticle Theory, *Phys. Rev. Lett.* **62**, 1169 (1989).
- [54] A. Oshlies, R. W. Godby, and R. J. Needs, *GW* self-energy calculations of carrier-induced band-gap narrowing in *n*-type silicon, *Phys. Rev. B* **51**, 1527 (1995).
- [55] P. Larson, M. Dvorak, and Z. Wu, Role of the plasmon-pole model in the *GW* approximation, *Phys. Rev. B* **88**, 125205 (2013).
- [56] C. A. Rozzi, D. Varsano, A. Marini, E. K. U. Gross, and A. Rubio, Exact Coulomb cutoff technique for supercell calculations, *Phys. Rev. B* **73**, 205119 (2006).
- [57] J. Wilhelm, D. Golze, L. Talirz, J. Hutter, and C. A. Pignedoli, Toward *GW* calculations on thousands of atoms, *J. Phys. Chem. Lett.* **9**, 306 (2018).
- [58] P. Umari, O. Petrenko, S. Taioli, and M. M. De Souza, Communication: Electronic band gaps of semiconducting zig-zag carbon nanotubes from many-body perturbation theory calculations, *J. Chem. Phys.* **136**, 181101 (2012).
- [59] T. Kotani, M. van Schilfgarde, S. V. Faleev, and A. Chantis, Quasiparticle self-consistent *GW* method: A short summary, *J. Phys. Condens. Matter* **19**, 365236 (2007).
- [60] M. Shishkin, M. Marsman, and G. Kresse, Accurate Quasiparticle Spectra from Self-Consistent *GW* Calculations with Vertex Corrections, *Phys. Rev. Lett.* **99**, 246403 (2007).

- [61] T. Pichler, M. Knupfer, M. S. Golden, J. Fink, A. Rinzler, and R. E. Smalley, Localized and Delocalized Electronic States in Single-Wall Carbon Nanotubes, *Phys. Rev. Lett.* **80**, 4729 (1998).
- [62] C. Kramberger, R. Hambach, C. Giorgetti, M. H. Rummeli, M. Knupfer, J. Fink, B. Büchner, L. Reining, E. Einarsson, S. Maruyama, F. Sottile, K. Hannewald, V. Olevano, A. G. Marinopoulos, and T. Pichler, Linear Plasmon Dispersion in Single-Wall Carbon Nanotubes and the Collective Excitation Spectrum of Graphene, *Phys. Rev. Lett.* **100**, 196803 (2008).
- [63] D. J. Mowbray, S. Segui, J. Gervasoni, Z. L. Mišković, and N. R. Arista, Plasmon excitations on a single-wall carbon nanotube by external charges: Two-dimensional, two-fluid hydrodynamic model, *Phys. Rev. B* **82**, 035405 (2010).